ANTIMONY-BASED TYPE-II SUPERLATTICE INFRARED PHOTODETECTORS ON INDIUM-ARSENIDE SUBSTRATES

BY

DANIEL YUAN ZUO

THESIS

Submitted in partial fulfillment of the requirements
for the degree of Master of Science in Electrical and Computer Engineering
in the Graduate College of the
University of Illinois at Urbana-Champaign, 2011

Urbana, Illinois

Adviser:

Professor Shun Lien Chuang

Abstract

The wide variety of applications for mid- and far-infrared detection has spurred the study of cutting-edge technologies for use in the next generation of detectors in place of the current systems, such as mercury cadmium telluride. While type-II superlattices offer a number of advantages in design and material quality, theoretical predictions of their high performance have yet to be realized. This work concentrates on novel designs, fabrication, and characterization of type-II superlattice infrared detectors.

In this work we present the first InAs/GaSb type-II superlattice photodetectors grown on an InAs substrate via metal-organic chemical vapor deposition. The design and fabrication of the devices are detailed, along with several characterization processes, including low-temperature electron beam induced current (EBIC) to study structural defects. Through this work, the optical absorption of the undoped substrate was shown to be significantly lower than that of GaSb. The detectors have a cutoff wavelength (50% responsivity) of 9.5 μm at 78 K. Their R_0A values are on the order of 10^{-2} Ωcm^2. The typical peak responsivity is 1.9 A/W, and the devices have a peak detectivity of 6.8×10^9 cm$\cdot$Hz$^{1/2}$/W at 78 K.

To my friends and family

Acknowledgments

I would like to thank those in my group for their contributions to this work. First of all, I thank Professor Shun Lien Chuang for his generous support and guidance after allowing me to work in the group. The past two years have allowed me to grow considerably as a scientist. I thank Martin Mandl, without whom I would not have received the proper training for the vast majority of the work presented in my thesis. I also wish to thank Thomas O'Brien and Benjamin Kesler for their help in proofreading my thesis. I thank all other members of the Optoelectronics Group at the University of Illinois at Urbana-Champaign for their help and support in reaching this point.

I thank Professor Russell Dupuis, Dr. Jae-Hyun Ryou, and Yong Huang at the Georgia Institute of Technology for providing the samples grown by MOCVD used in this work.

Additionally, I wish to thank all my family and friends for lending me support and wisdom both when I asked for it and when I did not.

Table of Contents

Chapter 1

Introduction

1.1 Infrared Radiation and Applications

The infrared (IR) regime of radiation is regarded with great interest among a variety of disciplines. Occupying the band of electromagnetic radiation between the visible spectrum and terahertz radiation (wavelengths of 0.7-300 μm), infrared radiation is abundant due to its transmission through the atmosphere and emission through black body radiation. There are two windows of infrared transmission within the atmosphere that are of particular interest: between 3 and 5 μm is the mid-wavelength infrared (MWIR) window, which is the primary focus of heat-seeking detectors used in guided missile technology. Between 8 and 14 μm is the long-wavelength infrared (LWIR) window, which is the primary window for thermal imaging applications. The two windows are separated by a strong gap of absorption caused by water in the atmosphere, as can be seen in the upper portion of Fig. 1.1. In this work we will concentrate on technologies for the detection of LWIR and MWIR radiation.

All objects emit radiation based on their temperature through a process called thermal radiation. This intensity is described in an ideal black body, which perfectly absorbs all radiation, by Planck's law:

$$I(\lambda, T) = \frac{2hc^2}{\lambda^5} \frac{1}{e^{\frac{hc}{\lambda k_B T}} - 1}. \tag{1.1}$$

In practice such an object does not exist, but Planck's law is a good estimate nonetheless. A human body at a temperature of 310 K has a peak emission wavelength of about 9.3 μm, placing it within the LWIR range. This makes the 8 to 14 μm window attractive for night vision applications. For example, forward-looking infrared (FLIR) systems utilize LWIR detection ([2],

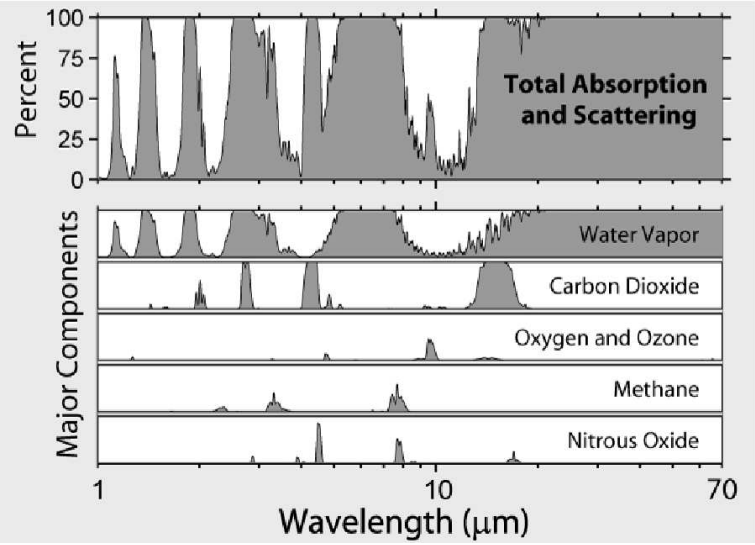

Figure 1.1: Atmospheric absorption spectra of the IR regime (top) and molecular absorption spectra of major contributing components. There are two windows allowing high transmissions: the MWIR and LWIR. Based on Ref. [1].

pp. 328–331). Similarly, the carbon dioxide emissions present in the plume of a jet engine make IR detection a major component of heat-seeking technologies ([2], pp. 363–400). Indeed, many molecules exhibit strong absorption behavior in the infrared regime, making IR detectors good candidates for spectroscopy applications as well.

1.2 IR Detection

Early IR detectors relied on the thermoelectric effect, discovered by Seebeck in 1821 [3], who went on to demonstrate the first thermocouple. Thermal detectors were sensitive to all wavelengths of infrared radiation, but also slow to respond and had low sensitivity. Most applications for IR detection, such as those mentioned previously, depend on fast response and a high signal-to-noise ratio (SNR), and so thermal detectors are poor candidates for most modern applications.

Photonic detectors were introduced later, in the twentieth century, starting with Case in 1917 [3]. Semiconductor-based detectors emerged in the 1960s, based on III-V, IV-VI, and II-VI alloys. A notable II-VI alloy is mercury

cadmium telluride (HgCdTe), or MCT. One of the most commonly used materials today, MCT exemplifies the flexibility that tunable bandgap materials provide by being able to accomodate a large range of IR wavelengths. However, it is not without its own set of drawbacks: material stability and cost of production are areas in which MCT leaves room for improvement, despite its exceptional performance.

A very promising new material system is the type-II superlattice (T2SL), which consists of thin alternating layers of III-V compounds which possess a type-II band edge alignment, such as InAs and $In_xGa_{1-x}Sb$. The benefits of the system include a highly flexible bandgap, a large electron effective mass [4] for lower tunneling currents, and suppressed Auger recombination thanks to strain-induced valence band splitting and conduction band flattening in the p- and n-regions, respectively [5]. The use of III-V materials is a considerable advantage, given the maturity of growth in this family and a wealth of material characterization options available. A diagram of an example band edge alignment can be seen in Fig. 1.2. The type-II alignment causes the electrons and holes to be confined in separate material layers, which in turn causes the effective band gap of the overall structure to be lower than the individual material bandgaps it comprises. Since this bandgap is sensitive to the material layer thickness due to confinement, it is possible to tune between 3 and 30 μm with an InAs/InGaSb SL. The optical absorption coefficient is comparable to MCT, and by leveraging mature III-V epitaxy techniques a superior uniformity can be achieved, which is of great importance for focal plane array (FPA) detectors.

1.3 Figures of Merit

Several figures of merit have been established [6, 7, 8] in order to characterize the performance of a detector and allow for comparison between various detector systems. The following section describes some of the commonly used figures.

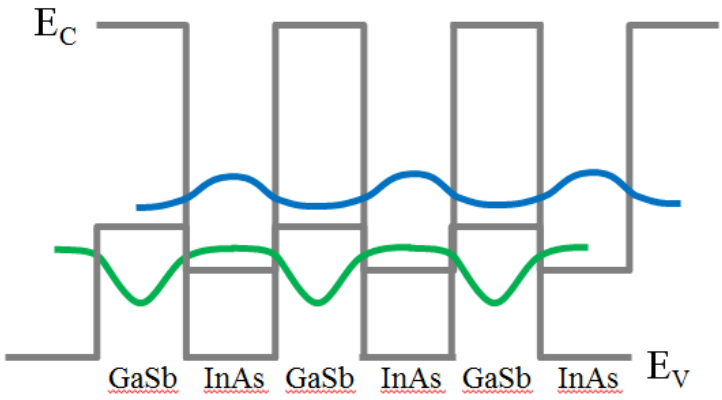

Figure 1.2: Band diagram of a flatband InAs/GaSb T2SL. In a type-II band edge alignment the valence band of one material has a higher energy than the conduction band of the other material. The thin layers allow for coupling between quantum wells, and the carriers are confined in separate layers resulting in a spatially indirect transition.

1.3.1 Responsivity

The spectral responsivity of a device is a measure of its sensitivity to radiation at a specific wavelength, defined by

$$R(\lambda) = \frac{I_s(\lambda)}{\Phi_e}, \tag{1.2}$$

where I_s is the measured photocurrent generated in the device, and Φ_e is the spectral radiant incident power. Further discussion of responsivity and the procurement of Φ_e can be found in section 2.3.3.

1.3.2 Quantum Efficiency

The quantum efficiency of a detector is the number of electron-hole pairs generated per incident photon. Quantum efficiency is a simpler figure that can be related to the responsivity of a device through a simple equation:

$$R(\lambda) = \frac{q\lambda}{hc}\eta(\lambda), \tag{1.3}$$

where q is the elementary charge, and η is the quantum efficiency.

1.3.3 Specific Detectivity

The specific detectivity is a universal figure of merit for detectors, and can be used to compare devices of varying size, bandwidth, and type. It is defined as

$$D^*(\lambda) = R(\lambda)\frac{\sqrt{A\Delta f}}{I_n}, \tag{1.4}$$

where A is the area of the detector, Δf is the electrical bandwidth, and I_n is the noise current. The unit of detectivity, cm·Hz$^{1/2}$/W, is called Jones.

1.3.4 Dynamic Impedance-Area Product (R_0A)

The most common type of photodetector is the photodiode. For an ideal photodiode at zero bias and in a low frequency regime, the noise current in the detector is dominated by thermal noise and is given by

$$I_n^2 = 4qI_s\Delta f = \frac{4kT}{R_0}\Delta f, \tag{1.5}$$

where I_s is the saturation current and R_0 is the resistance at zero bias voltage. Substituting this quantity into equation (1.4), the specific detectivity becomes:

$$D^*(\lambda) = R(\lambda)\sqrt{\frac{R_0A}{4kT}} = \eta\left(\frac{q\lambda}{2hc}\right)\sqrt{\frac{R_0A}{kT}}. \tag{1.6}$$

As an alternative to directly measuring the noise current of a device, the R_0A product is commonly used to quantify the noise of a photodiode and equation (1.6) is the Johnson noise-limited detectivity for detectors at zero bias.

In an ideal device the R_0A product reflects the properties of the bulk device. However, since defects and surface channels formed at the outer edges of the device can impact the performance significantly, the measured R_0A product can then be considered a combination of two internal resistances [9]:

$$\frac{1}{R_0A} = \frac{1}{R_0A_{bulk}} + \frac{1}{r_{surface}}\frac{P}{A}, \tag{1.7}$$

where R_0A_{bulk} defines the behavior of the bulk structure, $r_{surface}$ is the surface resistivity in Ωcm, and P is the device perimeter. The effect of the surface can be mitigated using passivation techniques.

1.3.5 Cutoff Wavelength

A useful figure of merit for a detector is the wavelength at which it begins to respond to incident radiation. Conversely, it is also the maximum wavelength that the detector is capable of measuring. Typically in a T2SL this is due to the effective bandgap, or the minimum transition energy between electron and hole states. The cutoff wavelength can be calculated by

$$\lambda_{co}(\mu\text{m}) = 1.24/E_g(\text{eV}), \tag{1.8}$$

where E_g is the bandgap in question, which can be obtained via theoretical modeling. The cutoff wavelength can also be experimentally observed in absorption and responsivity spectra, where the wavelength at which the signal drops to 50% of its initial step value is typically defined to be the cutoff.

1.4 State of the Art

Although considerable progress has been made with T2SL devices since the first proposal for their use in 1970 [10], they are still viewed as a next-generation technology since a number of performance-limiting issues have prevented them from reaching their full potential. Figure 1.3 shows a comparison between "Rule 07," a heuristic equation that describes the optimal performance of current MCT devices [11], and a selection of state-of-the-art T2SL detectors produced at the Naval Research Laboratory, which utilize advanced designs described in this section. While T2SL detectors have a theoretical performance limit superior to MCT, they are only recently beginning to match MCT detectors. Recent progress in advancing T2SL performance has leveraged the flexibility afforded by the stable III-V growth systems to produce novel SL structures. The following sections provide an overview of notable structures presented in recent literature.

1.4.1 W- and M- Structures

In an InAs/GaSb T2SL, the insertion of small AlSb layers creates barriers in the conduction and valence bands, which can be used to manipulate the confinement of carriers. Two applications of AlSb layers are W- and M-

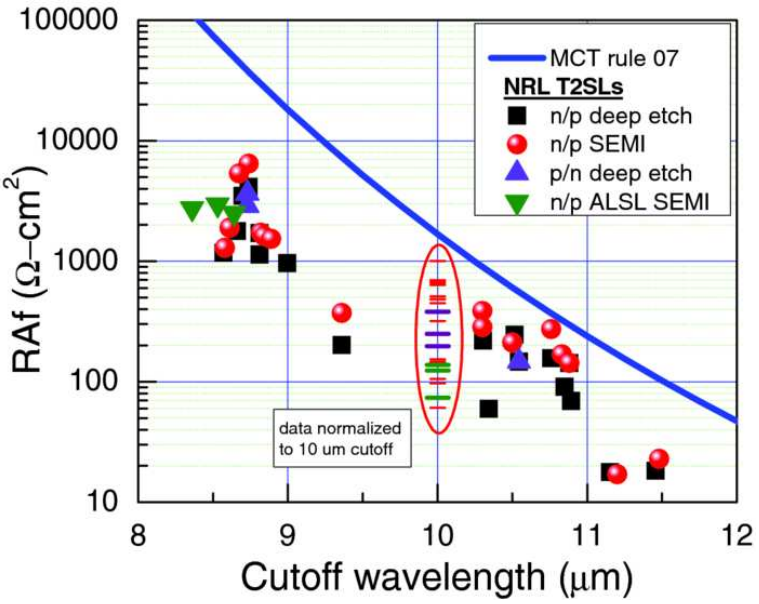

Figure 1.3: Comparison of the effective resistance area product for T2SL detectors fabricated by NRL and the Rule 07 heuristic perfomance for MCT detectors. After Ref. [12]

structures [13, 14] where the AlSb layer is inserted in the middle of the InAs layers or the GaSb layers, respectively. The nomenclature for the structures is derived from the shapes formed by the forbidden energies in the periodic structure. The layer in which the AlSb barrier is placed has an effect on its function. In the M-structure, the AlSb barrier increases the effective mass of electrons and lowers the tunneling current. In the case of the W-structure, the electrons are split up and confined in two separate regions, which forces their wave functions to have more overlap with those of the holes. The increased overlap enhances the optical absorption of the structure.

1.4.2 nBn and CBIRD

The use of barriers can also be extended to a larger scale, as seen in the nBn detector [15]. As the name implies, the device comprises an n-doped absorbing region, a large band-gap layer, and a thin n-doped contact layer. While the first proposal for this structure did not use SLs in the absorbing layer, later demonstrations [16, 17] proved that the overall design worked for T2SL arrangements. The barrier layer in the nBn design blocks electrons, the

majority carriers, and uses a flatband or slightly depleted region to generate photocurrent. The result is that the nBn device severely mitigates Shockley-Read-Hall recombination and tunneling current, two major contributors to noise in T2SL detectors. The minority carriers (holes) are unimpeded thanks to the design of the band edge alignment, and are responsible for carrying the photocurrent of the device. An extension of this technique is the complimentary barrier infrared detector (CBIRD) [18], which incorporates barriers on both sides of the absorbing region, which block the majority carriers and suppress noise-producing dark current. Unlike typical photodiode detectors, which operate in reverse voltage bias, the CBIRD is designed to operate in forward bias, where shot noise dominates. A CBIRD device reported by Ting et al. [18] in 2009 demonstrated an R_0A product of 14,000 Ωcm^2 at 77 K, with a cutoff around 10 μm.

1.4.3 Graded Bandgap Structures

Rather than using barriers, the high flexibility of the T2SL system allows for the use of graded bandgaps in the depletion region of a detector [19]. Since the effects of SRH recombination and tunneling depend exponentially on the band gap, the reduction of low-bandgap SL present under bias supresses the corresponding dark currents. The grading of the bandgap is accomplished by slightly altering the SL to change the effective bandgap gradually. Like barrier-structure devices, an adjacent flatband SL region is used to generate the photocurrent in order to keep the overall absorption competitive. The overall increase in bandgap in the depletion region also mitigates surface leakage current, since the larger bandgap structure interrupts the surface channel that forms in the more susceptible low-bandgap portion. By using adjusted SLs to mitigate the dark currents instead of a single high-bandgap material, the design of the structure is afforded more flexibility, especially with growth conditions and strain management to consider.

1.5 Thesis Overview

This work will focus on novel approaches to T2SL device production, as well as the methodology for fabricating and characterizing infrared detectors.

Rather than study specific structures, the baseline performance of standard $p-i-n$ photodiodes is evaluated in order to measure the potential of novel growth parameters.

Chapter 1 provides background information on infrared radiation and detection, and introduces important figures of merit used to describe the performance of detectors. It also describes some of the novel devices being produced as well as the state-of-the-art results.

Chapter 2 provides a description of the fabrication processes used to create the T2SL devices described in this work, and details the various characterization procedures used to study them. This includes an overview of the wet and dry etch methods for defining photodiode mesas, current-voltage response measurement, detector responsivity, and optical absorption coefficients.

Chapter 3 introduces a novel T2SL growth paradigm that uses an InAs substrate for the first time, achieved using metalorganic chemical vapor deposition (MOCVD). The advantages of the new substrate, both theoretical and observed, are discussed as well as the first InAs/GaSb T2SL photodiodes grown on an InAs substrate. The devices demonstrate a nearly four-fold increase in performance over the first generation of MOCVD-grown devices.

Chapter 4 discusses an advanced method for characterization of transport properties and defects within T2SL IR detectors, called electron-beam induced current (EBIC). Current progress in EBIC is presented for binary and ternary T2SL structures along with future work in EBIC.

Chapter 5 outlines the significant achievements of this work and future work to be done in order to further the baseline performance and quality of T2SL IR detectors.

Chapter 2

Device Fabrication and Characterization

2.1 T2SL Growth

The samples described in this work were grown at the Georgia Institute of Technology, by metal-organic chemical vapor deposition (MOCVD). This technique differs from the standard molecular beam epitaxy (MBE) in that the material layers are deposited through chemical reactions under high pressure, whereas MBE uses heated sources to deposit pure materials on a target under high vacuum. Whereas MBE has been the exclusive method of growth for T2SL studies, it is costly and slow compared to MOCVD. Since MOCVD is desirable for production-level output, the demonstration of high-performance T2SL detectors is key to the development of the technology. MOCVD caries along with it a set of of unique considerations for T2SL structure design, which will be detailed in chapter 3.

2.2 Fabrication of Detectors

The samples were used to define $p-i-n$ photodiodes using a two-step UV photolithography process. The samples are first etched to form a series of square mesas with various side lengths: 150 μm, 200 μm, 300 μm, 400 μm. The mask used to etch the mesas was comprised of AZ 5214E photoresist (PR), which is exposed to a mercury lamp in a Karl Suss pattern aligner. The samples are etched down to the bottom contact layer through one of two methods. Since the designs do not incorporate an etching stop layer (and since this is not possible during a dry etch), precise control of the etching depth is necessary to avoid removing the bottom contact layer.

After the etch step was completed, the etching mask was removed and the

sample was thoroughly cleaned to remove residual PR and etchant byproducts. A second PR mask was applied to the sample to prevent portions of the detectors from being contacted by metal. Using e-beam evaporation, metal contacts comprised of Ti/Pt/Au layers were deposited on the sample. The metals form ohmic contacts with the n-InAs and p-GaSb device layers, eliminating the need for any annealing process. By using a solution to remove the underlying PR, areas where this contact was unwanted (such as the exposed SL sidewalls) were stripped of metal. At the top of the detectors, rectangular windows were left in the metal contact to allow for radiation to pass through to the active regions.

To prepare the samples for characterization, they were mounted in a ceramic chip carrier using high purity silver paint. The contacts with individual detectors were made using ball-bonded gold wire.

2.2.1 Wet Etching

Chemical wet etching is a technique that lends itself to research applications, as it requires very little equipment to apply and is easy to control. However, it tends to etch material in an isotropic manner, undercutting the masks used in photolithography. This can lead to issues in applications that rely on extremely small feature sizes, but the detectors in this work were large enough that this was not an issue. The solution used to etch the samples was comprised of citric acid, phosphoric acid, and hydrogen peroxide. The citric acid etches InAs layers, and the phosphoric acid etches the GaSb layers. The hydrogen peroxide is introduced as an oxidizing agent. Since InAs and GaSb comprise all of the materials present in the sample, and the speed at which the sample is etched varies based on the material composition with respect to the solution mixture, the rate of etching was carefully controlled through repeated testing in order to prevent over- or under-etching the sample. Using wet etching the sample was etched as a rate of approximately 50 nm/min.

2.2.2 Dry Etching

Dry etching is an alternative method to define the mesas of the photodiodes. The necessary equipment is expensive and the process is inherently difficult

to set up and control, due to the complexity of operation. However, once established it is much faster than wet etching and allows for anisotropic etch profiles; thus it is the method favored by the industry for producing massive quantities of devices. The disadvantage is that the bombardment of ions can damage the sample and create defects and trap states at the surface, which can degrade performance.

Several samples were fabricated using dry etch, in a process called inductively coupled plasma reactive ion etching (ICP RIE). During this process, a plasma is generated by subjecting a gas to high frequency RF electrical field. A DC voltage is applied to the chamber containing the plasma and the sample, which causes the ions in the plasma to bombard the sample, removing exposed portions through either a chemical reaction or by imparting kinetic energy. Since the conditions in the chamber during RIE are not suitable for PR masks, which burn and become difficult to remove, the process requires that the mask be formed out of a different material. In this work, a layer of SiN was deposited on the sample prior to photolithography, which was patterned through lithography and a Freon RIE that did not burn the PR. Afterwards, the SiN mask was removed and the process continued as described earlier. Using ICP RIE the samples were etched at a much faster rate, approximately 800 nm/min.

2.3 Characterization

Characterization of the detectors was achieved using a Janis ST-100 cryostat, which allows each sample to be tested at liquid nitrogen (78 K) or lower temperatures, as well as up to room temperature. The samples were mounted on a cold finger inside the cryostat and soldered to the built-in wiring, allowing for external current measurement. To allow for testing of responsivity and absorption, the cryostat was fitted with ZnSe windows that transmitted IR radiation up to 22 μm.

2.3.1 *I-V* Response

The *I-V* curves of the detectors were measured with an HP 4145B semiconductor parameter analyzer. This measurement allows the R_0A product to

be calculated by dividing the detector area by the slope of the curve at zero bias. In order to ensure that the detector is dominated by thermal noise, the cryostat was surrounded with tinfoil to prevent background IR radiation from affecting the measurement.

2.3.2 Fourier Transform Infrared Spectroscopy

The optical characterization of the various samples revolves around a technique called Fourier transform IR (FTIR) spectroscopy. FTIR allows for the measurement of a wide spectrum of radiation without the need for a tunable light source, making it a popular measurement tool.

The fundamental component of a FTIR spectrometer is an interferometer, shown in Fig. 2.1. A radiation source, such as a globar, with a broad radiation spectrum is directed at a beamsplitter which sends the two halves of the beam toward mirrors. One of the mirrors is able to move, altering the beam path length. The two halves recombine back at the beamsplitter and pass through the sample under test before being recorded by a detector. Based on the difference in path lengths between the two mirrors, the light will constructively and destructively interfere at different wavelengths. As a result, the time domain intensity distribution, or interferogram, can be related to the frequency-domain response of the system by a Fourier transformation.

2.3.3 Responsivity

To obtain the responsivity curve of a detector, it was placed at the focus of the beam emitted from a Bomem DA-8 FTIR spectrometer and manually connected to the current measurement circuit of the spectrometer. The spectrometer is equipped with a KBr beamsplitter and a globar source, which allow measurements to be made in the MWIR and LWIR regimes. Each measurement was made at 4 cm^{-1} resolution and averaged over at least 50 scans. The number of scans usually depends on the signal-to-noise ratio of the detector— a lower quality detector will usually require more scans in order to clean up the noise in the responsivity curve.

Because there is no information in the spectrum about the incident power, the curve obtained from the DA-8 is simply a relative responsivity curve. To

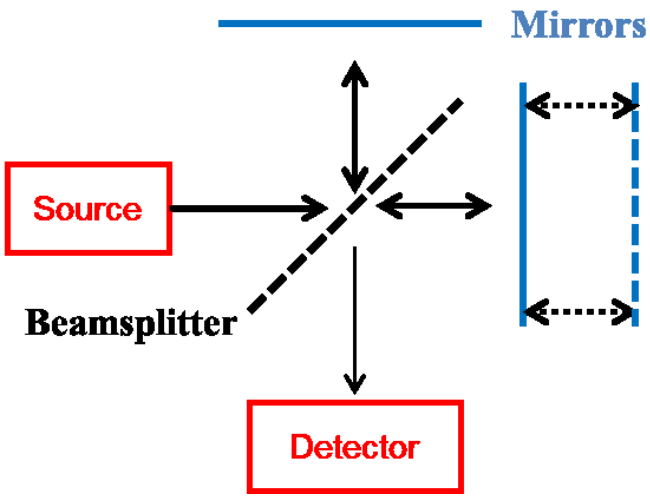

Figure 2.1: Schematic of the interometer central to the operation of the FTIR spectrometer. A movable mirror is used to alter the interference of the source beam and create an interferogram for interpretation.

obtain the values of responsivity the curves needed to be calibrated through a secondary measurement. This was accomplished using a Mikron M 305 blackbody source setup as illustrated in Fig. 2.2. The blackbody radiation, set at 1000 °C, passes through an optical chopper and a circular aperture (diameter a), and passes through an optical spike filter before reaching the detector. The rms photocurrent i_p picked up is measured using a Stanford SR650 lock-in amplifier based on the modulation frequency of the chopper. Provided that the distance from the aperture to the detector d is large compared to the aperture diameter, the incident rms power can be calculated as

$$\Phi_d = \pi \left(\frac{a}{2d}\right)^2 A_{opt} c_m t_w \int_{k_1}^{k2} \frac{k^3 h c^2}{8\pi^4 \left(e^{hck/2\pi k_B T} - 1\right)} t_f(k) dk, \qquad (2.1)$$

where A_{opt} is the exposed surface area of the detector, c_m is the modulation due to the optical chopper [6], t_w is the transmission of the cryostat window, and t_f is the transmission of the filter with cutoff wavenumbers k_1 and k_2. The responsivity at the spike filter wavelength was then calculated as $R_{\lambda_{spike}} = i_p/\Phi_d$ and the relative responsivity curve can be calibrated to this value.

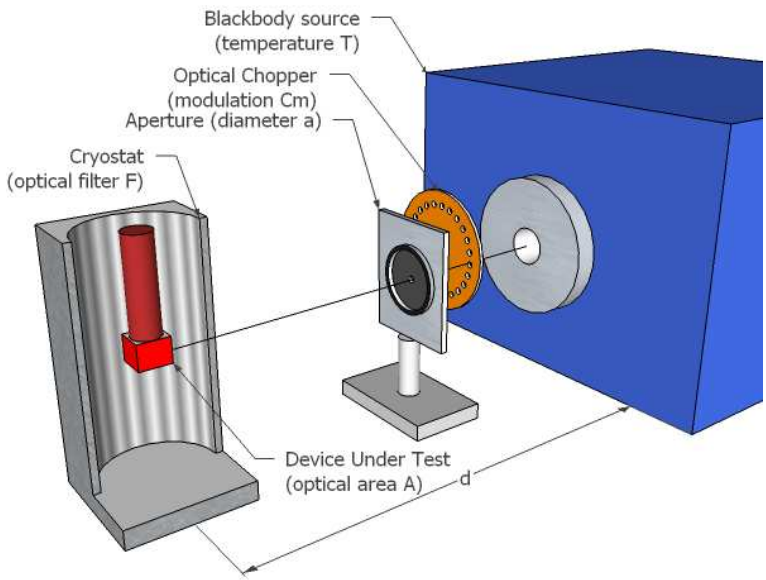

Figure 2.2: Schematic of the blackbody calibration setup used to measure responsivity. The optical chopper allows the photocurrent induced by the blackbody radiation to be isolated using a lock-in technique.

2.3.4 Optical Absorption

The FTIR is capable of measuring the optical absorption coefficient of a sample, provided one is willing to spend some extra time on sample processing and data analysis. The sample to be measured has been split into two with one portion having the epilayer etched away and the other being preserved. Light either passes through the bare substrate (T_1) or through the sample as well as the substrate (T_2) before being picked up by the side-mounted detector of the FTIR.

The objective is to extract the optical absorption of the material under study, eliminating all other sources of power attenuation from analysis. This is the reason for measuring the two different sample conditions, one with the material being studied and one without. Assuming the the top of the structure being studied and the substrate are the same material, one can safely assume that the transmission spectra obtained from the FTIR T_1 and T_2 are related by the absorption of the studied structure:

$$T_2 = T_1 \cdot \exp -\alpha L_{etch}, \tag{2.2}$$

where α is the optical absorption spectrum we wish to extract and L_{etch} is the depth of the removed material. This simple relationship assumes that the differences in interface effects between the two regions is at worst negligible; if that is not the case then the absorption coefficient will produce misleading results. It is extracted from the two base spectra:

$$\alpha = ln\left(\frac{T_1}{T_2}\right)/L_{etch}. \tag{2.3}$$

Chapter 3

Type-II Superlattice Grown on an InAs Substrate by Metalorganic Chemical Vapor Deposition

3.1 Growth and Fabrication

Until recently the exclusive method of growth for InAs/GaSb T2SL IR detectors had been molecular beam epitaxy (MBE). MBE lends itself to research applications, due to the extreme precision it affords to the growth of SL structures: the thickness of the layers can be controlled down to half a monolayer. This precision is desirable since SL structures are sensitive to minute changes in layer dimensions. However, MBE systems are prohibitively expensive for any application outside of research and prototyping, given the large costs of upkeep and very slow output rates. To demonstrate the viability of T2SL IR detectors in the next generation of commercially available products, a set of InAs/GaSb T2SL structures were grown via metalorganic chemical vapor deposition (MOCVD) on conventional GaSb substrates [20]. Despite successfully demonstrating that the resulting detectors were viable, the growth process was complicated and delicate, requiring the use of intentionally inserted interfacial layers between InAs and GaSb in order to manage the strain of growing InAs on the GaSb-matched lattice. Fig. 3.1 shows the lattice constants of the related materials. InAs is tensile strained on GaSb, and the formation of GaAs at the interface between InAs and GaSb can lead to significant tensile strain (GaAs— 5.65 Å, InAs— 6.06 Å, GaSb— 6.10 Å). In MBE, InSb interfacial layers are an effective solution, but the operating temperatures in MOCVD are close to the melting point of InSb, requiring a different solution. In previous work [21], a mixed interfacial scheme of InAs→InAsSb→InGaSb→GaSb→InGaSb→InAsSb→InAs was used to balance the strain. This method required very strict control of the growth process, since each layer alters the overall superlattice.

It is advantageous to instead use an InAs substrate for the detector. There

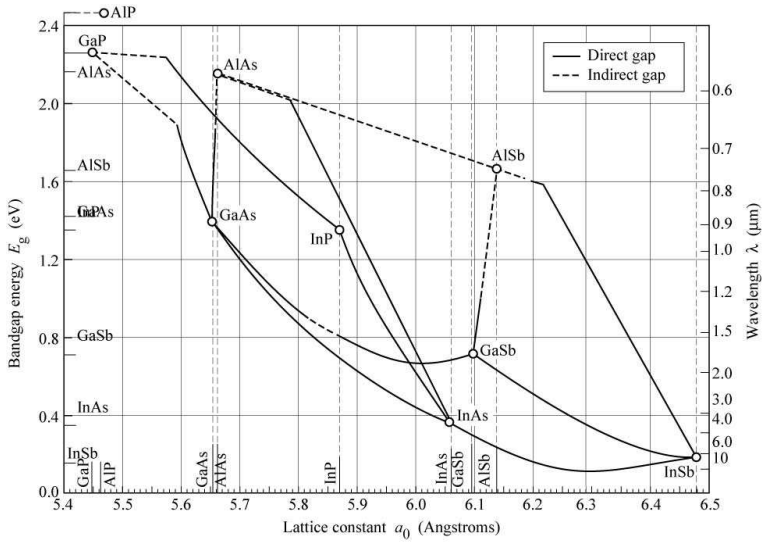

Figure 3.1: Diagram of bandgap energy versus lattice constant for various III-V semiconductor compounds. After Ref. [22]

are several reasons behind this approach. With regard to the strain management: since the SL structure is being matched to InAs, the compressive strain in the GaSb layers can be counterbalanced by intentionally allowing interfacial layers of GaAs to form, eliminating the need for a complex layer switching scheme. Additionally, the use of InAs substrates should allow for improved flip-chip designs for detectors since the optical absorption of InAs is lower in the MWIR and LWIR regimes than GaSb, which is experimentally verified later in this chapter. In order to demonstrate this, several detector designs were created based on 8-band $k \cdot p$ theory [23, 24]. The latest design, which is reported in this work, utilized 5.14 nm thick InAs layers and 2.43 nm thick GaSb layers. A 300 nm thick n^+-InAs layer ($n \sim 2 \times 10^{18}$ cm^{-3}) was grown on the n-InAs substrate, which was doped at background levels ($n \sim 2 \times 10^{16}$ cm^{-3}). This was followed by the SL $n-i-p$ structure, starting with 60 periods of SL with graded n-doping ($n \sim 2 \times 10^{18}$ to 1×10^{16} cm^{-3}) followed by 200 periods of not intentionally doped SL, and 60 periods of graded p-doped SL ($p \sim 1 \times 10^{16}$ to 3.8×10^{18} cm^{-3}). A top contact layer was formed with 50 nm of p^+-GaSb ($p \sim 3.8 \times 10^{18}$ cm^{-3}). More details concerning the growth process are expected to be published. Fig. 3.2 shows the layer details for the overall structure.

The devices were fabricated by defining mesas via a dry etch, as described

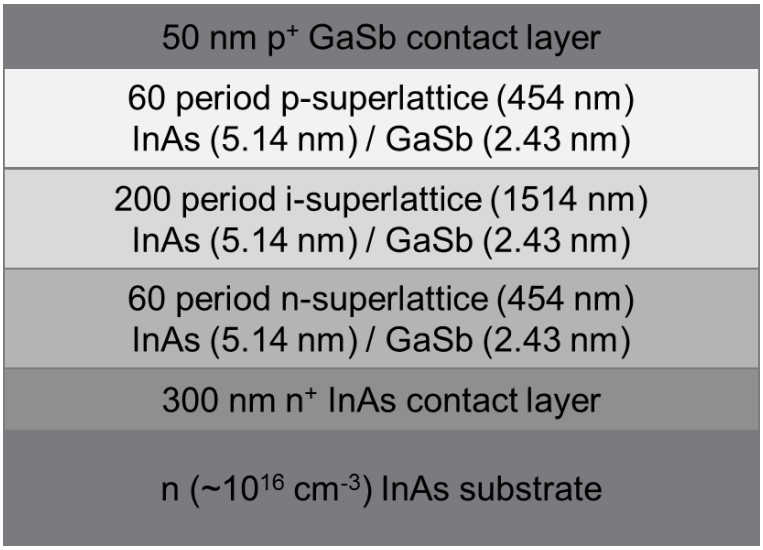

Figure 3.2: Schematic of the $n-i-p$ photodiode structure grown on an undoped InAs (001) substrate. Doping concentrations are as follows: n^+-InAs $\sim 2\times10^{18}$ cm^{-3}, n-SL graded $\sim 2\times10^{18}$ to 1×10^{16} cm^{-3}, p-SL graded $\sim 1\times10^{16}$ to 3.8×10^{18} cm^{-3}, p^+-GaSb $\sim 3.8\times10^{18}$ cm^{-3}.

in Chapter 2. In all, the fabrication can provide up to 60 total devices, although the number of viable devices will depend on the quality of metal lift-off and wire bonding. Fig. 3.3 shows the etched mesas in scanning electron microscope (SEM) images. While the sidewalls appear to be rough due to the RIE etch, the surface of the detector appears very smooth, lacking the hillocks and dislocation lines that appeared in the first generation of MOCVD-grown T2SL detectors [25]. This is evidence of higher stability present in the structure, although stronger confirmation of this can be found using precision measurements like transmission electron microscopy (TEM) and X-ray diffraction (XRD).

3.2 Characterization

3.2.1 Electrical

A number of mesas were contacted via ball-bonding for characterization. Their I-V curves were taken with the HP 4145B analyzer, allowing their R_0A products to be determined. Table 3.1 lists the aggregated R_0A measurements

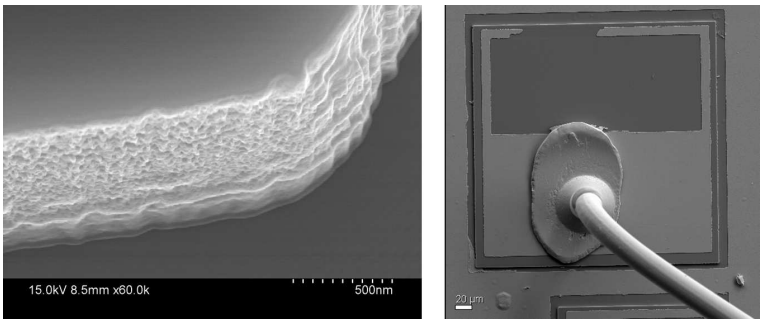

Figure 3.3: SEM images of the InAs/GaSb T2SL sample during processing. A magnified image (left) shows the sidewall of a mesa, while an entire mesa (right) with metal contact and ball bond applied are shown as a demonstration.

Table 3.1: Calculated R_0A products for the InAs substrate detectors according to their perimeter-to-area ratio (P/A). The standard deviation (SD) is shown as well as the number of detectors measured (N).

P/A (cm^{-1})	Mean R_0A ($\Omega\mathrm{cm}^2$)	SD ($\Omega\mathrm{cm}^2$)	N
100	5.24	1.78	3
133	4.92	1.05	4
200	2.78	0.40	3
267	1.72	0.36	4

from all working devices.

Plots of the current normalized by detector area and the RA product based on bias voltage for the larger devices (300 $\times$ 300 and 400 $\times$ 400 $\mu\mathrm{m}^2$) are shown in Fig. 3.4. Overall, the detectors exhibit R_0A products roughly two times better on average than the previous generation of MOCVD-grown detectors (GaSb substrates). By normalizing the current, a trend is visible in the performance of the detector compared to its area. The smaller mesas have smaller R_0A products on average (4.6 versus 5.2 $\times$ 10^{-2} $\Omega\mathrm{cm}^2$). This suggests that the detectors are limited by surface channel current near zero bias, which affects the overall resistance of the photodiode relative to the ratio of the diode's perimeter to its area [9]. The smaller the ratio, the larger the effect of the surface channel.

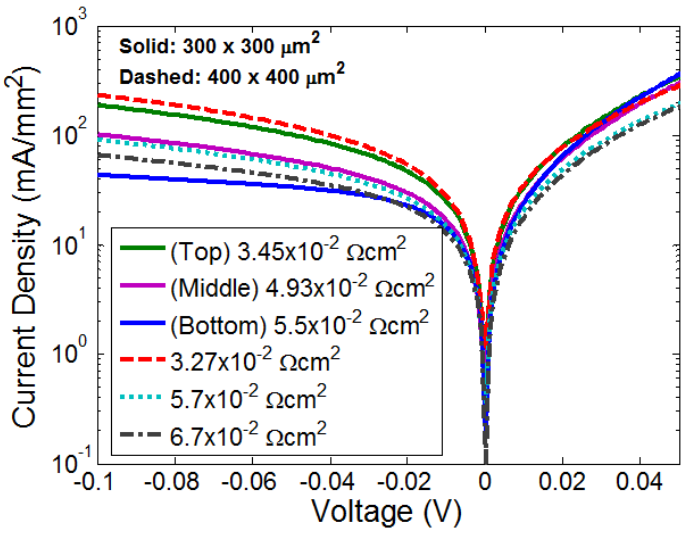

(a)

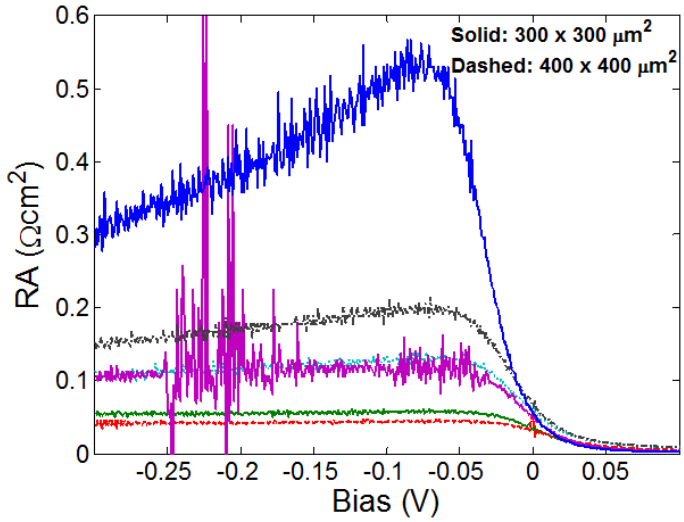

(b)

Figure 3.4: Electrical response curves of the InAs substrate-based T2SL detectors, containing two mesa sizes: 300 × 300 μm^2 (solid lines) and 400 × 400 μm^2 (dashed lines). (a) Current density plot, normalized with detector area. (b) Effective resistance area product calculated through finite difference.

In reverse bias there is no distinguishable trend with respect to device area. Based on the dark current model proposed by Mou et al. [8], the reverse bias dark current is limited by trap-assisted tunneling, which supports this observation, given that bulk defects will dominate unless the structure is of extremely high quality. An outlier is visible in the resistance area product

data with much larger overall resistance in reverse bias. Since these data are confirmed by multiple I-V measurements, it is likely that the quality of processing varies widely among individual detectors.

This observation was confirmed in a wider study of the devices which included the smaller areas (200 $\times$ 200 and 150 $\times$ 150 μm^2). Based on (1.7), the inverse R_0A products of all measured devices were plotted based on their perimeter-to-area ratio (P/A). The result is shown in Fig. 3.5. A significant dependence on the ratio P/A was observed, suggesting that surface currents were a large factor in the performance of the devices, even at 78 K. By fitting a least squares linear equation to the data (dashed line) and extracting the relevant parameters, the bulk R_0A product was estimated as 10.8 $\times$ 10^{-2} Ωcm^2 and the surface resistivity as 4 $\times$ 10^{-4} Ωcm.

3.2.2 Optical

The relative responsivity curves were measured through FTIR spectroscopy using the Bomem DA-8 spectrometer. Fig. 3.6 shows the curve obtained from a typical device at 78 K, with the absolute value of the responsivity calibrated through (2.1) using a blackbody source at 1000 °C and with a spike filter at 4.8 μm. The curve includes some of the transmission characteristics of the FTIR system: the KBr beamsplitter response drops off for higher frequencies, resulting in an artificial slope at the left portion of the curve, while the atmospheric absorption of CO_2 and H_2O can be seen at 4 μm and 5-8 μm, respectively. The resolution was set to 4 cm^{-1} and the spectra of 100 scans were averaged to obtain the data. A robust LOWESS smoothing algorithm was applied using data analysis software (solid line) in order to approximate the true signal, given the presence of noise. The 50% cutoff wavelength of the device, 9.5 μm, agrees well with the intended cutoff of the design, 10.9 μm. The discrepancy can be attributed to the presence of GaAs interfacial layers, which were not considered in the modeling process, and some uncertainty in the actual thicknesses of the InAs/GaSb layers. This is reinforced by the shallow slope of the cutoff, which suggests significant linewidth broadening in the optical absorption in comparison to devices produced via MBE [26, 17, 27].

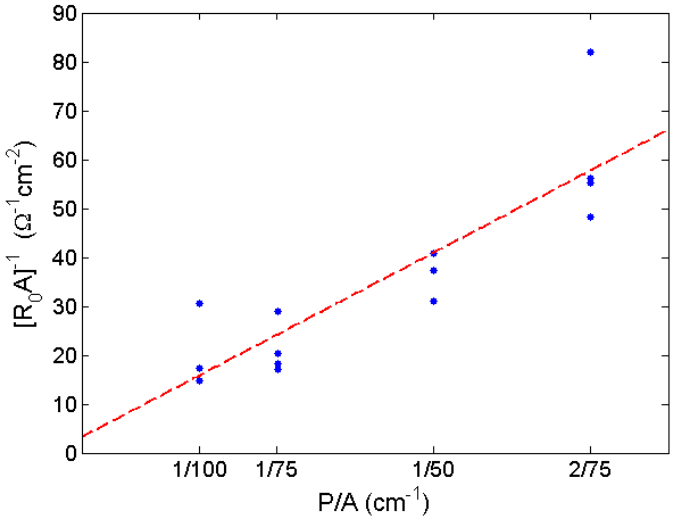

Figure 3.5: Inverse R_0A products versus the perimiter-to-area ratio P/A for the fabricated detectors on an InAs substrate obtained at 78 K. The significant variation with respect to P/A demonstrates that surface leakage current is a limiting factor for the detectors. A linear least-squares fit is also shown (dashed line), estimating the dependence of the resistance on P/A.

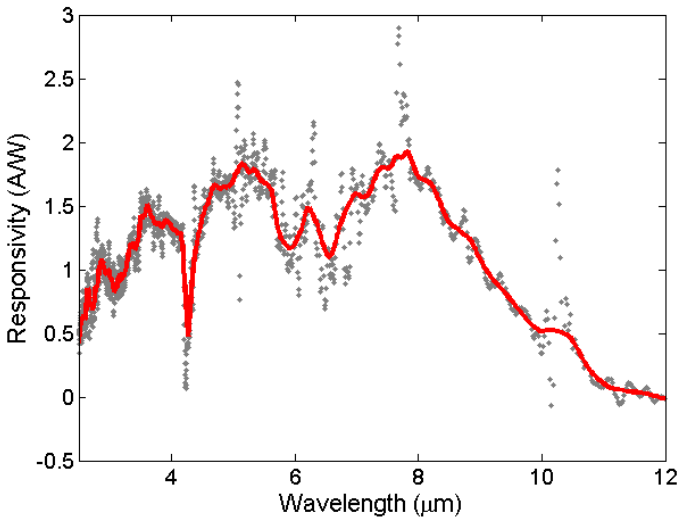

Figure 3.6: Optical responsivity measurement of a typical detector (size 300 μm) taken at 78 K. An averaged curve (solid line) is shown with artificial peaks removed. The dips around 4 μm and 6 μm are a result of atmospheric absorption. The dropoff due to the KBr beamsplitter response is visible at the left.

The peak D^* value of the device was measured at 6.8×10^9 Jones, which is a significant improvement over the previous generation— a roughly four-fold increase [20]. However, this improvement still leaves the device one or two orders of magnitude below state-of-the-art MBE devices [26, 17, 27]. Despite being very encouraging for MOCVD growth, the results also demonstrate the performance gap that still exists between MOCVD and MBE growth. Further work to optimize growth conditions as well as the susceptibility of T2SL designs to lattice imperfections will be necessary to achieve competitive results, both with respect to other T2SL results and MCT detectors.

3.2.3 Substrate Absorption

In addition to the detectors, two substrate samples, unintentionally doped InAs and GaSb, were measured to compare their optical absorption in the IR regime and to verify the improved substrate transparency. Each sample was broken up into two pieces; one of which was mechanically polished to remove a portion of the material. The other piece was also polished, but only to produce the same surface quality as the lapped piece. The InAs samples were then 500 μm and 250 μm thick, while the GaSb samples were 500 μm and 450 μm thick. The difference in lengths, measured by a high-precision caliper, was tailored to the expected difference in absorption: in order to produce a measurable change in transmission, the InAs sample, which was anticipated to have lower absorption, was polished further than the GaSb sample.

After polishing and measuring thicknesses, the samples were placed on individual apertures for optical isolation and mounted in a Janis cryostat for low pressure and low temperature conditions. Using a Bomem DA8 FTIR the transmission spectra for each sample were measured at varying temperatures. To ensure proper alignment of the samples, a lock-in technique was applied using an optical chopper to modulate the signal from the FTIR. Fig. 3.7 illustrates the absorption extraction process.

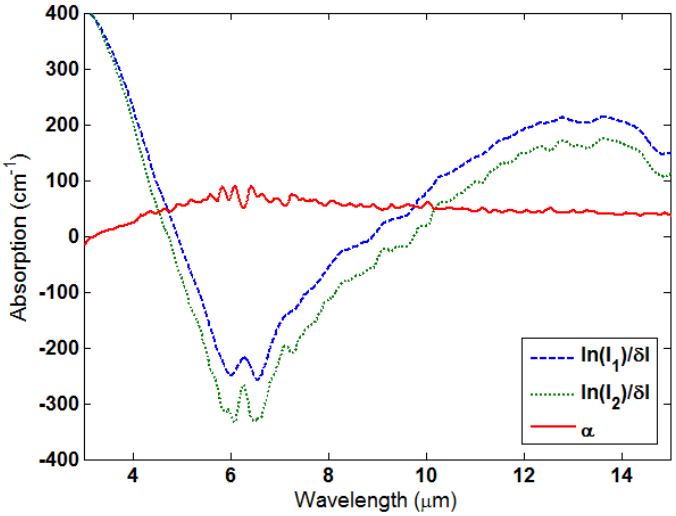

(a)

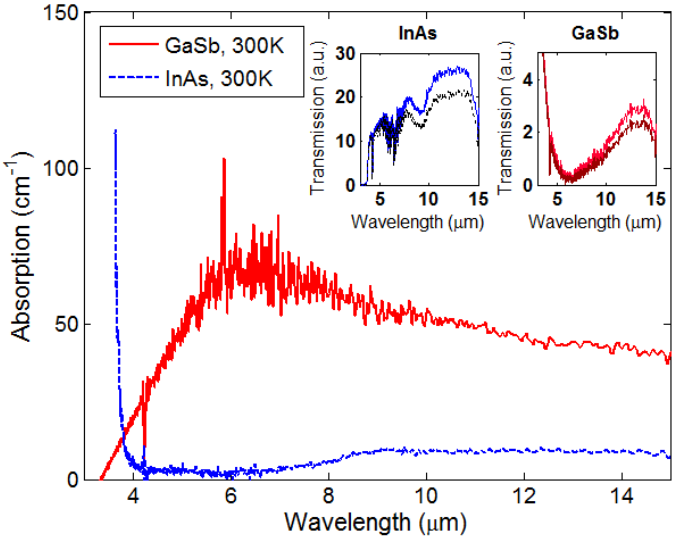

(b)

Figure 3.7: Absorption measurement data for the undoped bulk substrate samples. (a) Illustration curves depicting the mathematical calculations for extracting absorption from raw transmission data. The curves are smoothed to ease comparison. (b) Unaltered absorption data extracted for both InAs and GaSb substrates at room temperature. The InAs substrate demonstrates higher transparency in MWIR and LWIR. Insets: raw transmission data used to obtain absorption curves.

Fig. 3.7(a) shows the raw data obtained from the GaSb samples to illustrate the absorption extraction process. The raw spectra are presented in log-scale and normalized by the difference in thicknesses, 50 μm. Thus the difference between the two curves is the absorption coefficient, which is shown in Fig. 3.7(b). In Fig. 3.7(a), the curves have been smoothed to ease interpretation and comparison. Fig. 3.7(b) displays a comparison of the (unsmoothed) absorption coefficients of both InAs and GaSb at 300 K. The insets of the second plot show the linear scale raw transmission spectra used to obtain the absorption coefficients.

As expected, although the band gap energy of InAs is at the end of the mid-wave IR window, it exhibits much lower absorption than GaSb for all wavelengths longer than 4 μm. Careful consideration of the InAs band edge is thus necessary for mid-wave applications.

Chapter 4

Electron Beam Induced Current Study

4.1 Introduction

Electron induced beam current (EBIC) is a widely used technique for characterizing the carrier diffusion in a material. The reasons for its use include a wide range of applicable materials and devices; in addition, the tool required for the technique, a scanning electron microscope (SEM), is already commonly used for material characterization. Its first demonstration was by Lander et al. [28] in 1963, who first demonstrated the application of an EBIC signal for imaging of crystal defects. Many studies on different materials have been done since then, particularly on silicon [29, 30, 31]. This section focuses on our recent work using EBIC to study the properties of T2SL structures and to illustrate the variety of applications the technique has.

4.2 Basic Principles

In the EBIC technique, electrons are generated and focused into a beam by the SEM. The electrons, which typically have energies on the order of several kV, interact with the material in two ways: elastic and inelastic scattering [32]. In elastic scattering, the incident electrons are deflected by the lattice points and change trajectories. Since there is no energy transfer, this causes the electrons to disperse, effectively allowing them to interact with the material in a volume much larger than the original ingress point. This region is called the generation volume or interaction volume. When the electrons impart energy upon the electrons in the material, more interesting results occur. By exciting an electron from the valence band into the conduction band, an electron-hole pair is created. In regular SEM imaging, electrons

which are given enough energy to ionize and escape the surface are picked up to form an image of the sample. However, with the presence of a built-in electric field, the electron-hole pairs can be separated to produce specimen current. By amplifying this current and using it as a signal, an EBIC image is formed. Because defects can reduce the diffusion lengths of carriers, an EBIC image can be used to directly observe their presence in the material.

4.3 Contrast Analysis of Defects in SL Structures

In its most basic form, the image produced by EBIC can provide qualitative information about the presence and severity of electrically active defects. In this work, EBIC images of undoped T2SL samples were taken to investigate the presence of active defects. The sample in question was made up of 50 periods of undoped SLs comprised of InAs(7 nm) and $InAs_{0.6}Sb_{0.4}$(2 nm). The samples were grown by MOCVD as an alternative to InAs/GaSb in order to simplify the strain balancing process on GaSb substrates, as most compositions of InAsSb are compressively strained on GaSb to counterbalance InAs and the potential formation of GaAs.

Since the sample was not doped, to form a region to collect current a 300 nm thick layer of gold was deposited on the top of the exposed superlattice (InAs). Gold was chosen specifically in order to form a Schottky contact, which would provide the necessary built-in field through Fermi level pinning (in typical detector fabrication processes, depositing titanium first avoids this situation). The layer of gold covered only a portion of the sample and formed the first contact, while another contact was made by bonding the bottom of the substrate with silver paint to a gold-plated ceramic chip carrier. The contacts were verified by taking an I-V curve to observe diode behavior. The SEM and EBIC images were taken at liquid He temperature ($\sim$6 K) using a JEOL 6060LV SEM equipped with a cold stage and electrical contacts. The sample was kept cool by constantly flowing liquid helium through the stage while inside the chamber of the SEM. The electrical signal for EBIC imaging was amplified with a current amplifier and passed to a scanning circuit used to convert signals into images based on the scan position of the electron beam. Figure 4.1 displays representative images taken from a top-down view of a region near the Schottky contact.

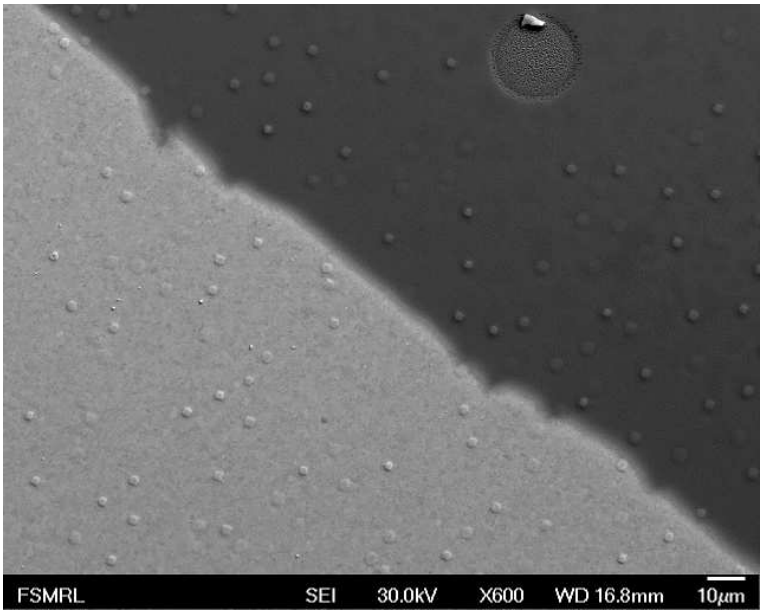

(a)

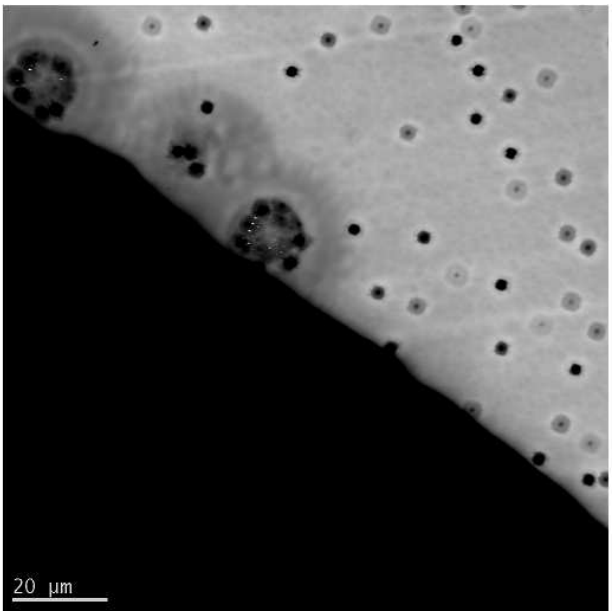

(b)

Figure 4.1: (a) SEM image and (b) EBIC image of the top surface of an InAs/InAsSb SL taken at 6 K. Visible in the lower left region of both images is the area in which gold has been deposited. Also featured in both images are a number of round aberrations, due to threading dislocations within the structure. The bottom image has been adjusted for levels and contrast in order to enhance the visibility of the smaller defects.

The images were taken at the boundary between the gold contact and exposed InAs layer. In the SEM image, the gold is prominently visible in the lower left region thanks to its high Z value, meaning that a greater number of backscattered electrons are produced and detected. This leads to the region appearing white in the image. In the EBIC image, the gold region appears black since the high Z prevents electrons from reaching the sample and generating current. Visible in both images are round aberrations on the surface of the sample that are present even beneath the gold layer, suggesting that they were present before processing of the sample began. What is significant about these round features is that they also feature prominently in the EBIC image, suggesting that they have a significant impact on the generation of carriers. The dark spots indicate that carriers generated within those areas are being captured and thus not contributing to current. This suggests the presence of a trap energy state, which would imply that the spots correspond to defects within the material. Their visibility at the surface of the sample and at varying depths (the darkness of the spots differs in the EBIC image, suggesting some spots are not as deep) also means that the defects propagate upward during growth, which enhances their severity. Figure 4.2 shows SEM images demonstrating the uniformity and population of defects visible on the surface. Based on the images gathered, a surface defect density of 5×10^6 cm^{-2} was estimated. Given the ubiquity of these defects, it is apparent that the growth conditions were less than ideal, perhaps due to the disproportionate amount of InAs relative to InAsSb. Further confirmation of the presence of defects can be performed using cross-sectional TEM measurements.

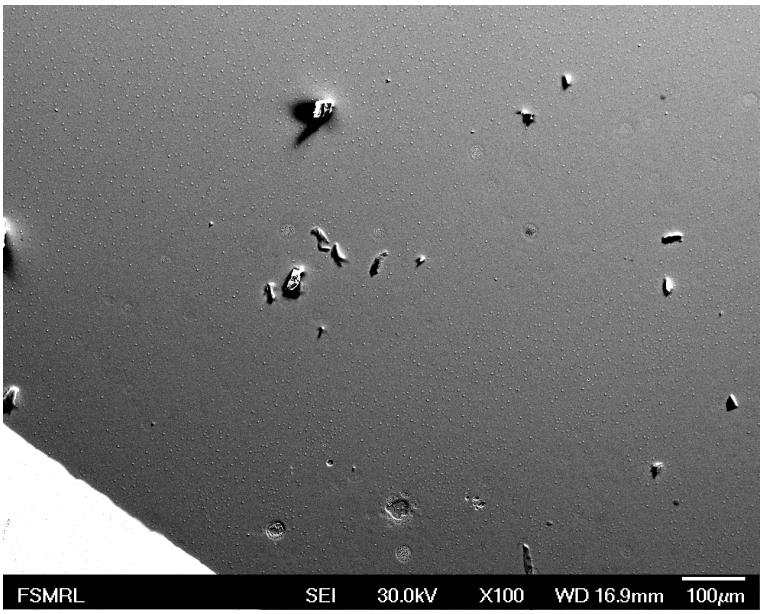

(a)

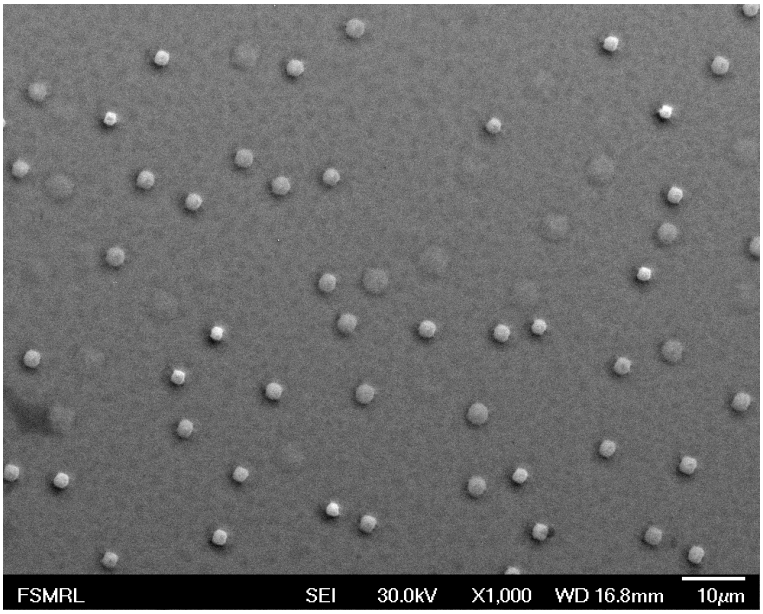

(b)

Figure 4.2: Representative SEM images of the surface of the InAs/InAsSb sample. (Top) Low-magnification SEM image of the sample surface, showing the uniformity of surface defect population. The defects, which are no larger than several pixels in this image, are present in all regions regardless of distance from the gold Schottky contact (bottom-left). (Bottom) High-magnification image of the surface defects. By counting the visible deformations in the image shown and others like it, a surface defect density of 5×10^6 cm^{-2} was estimated.

4.4 Contrast Analysis of Carrier Transport in T2SL Photodiodes

The EBIC technique was also applied to a functional detector in order to evaluate the transport of carriers within the SL structure. The InAs/GaSb detectors grown on InAs substrates were images using the previously described setup. The samples were positioned so that the electron beam was incident along the direction of growth in order to study in-plane carrier transport. Figure 4.3 shows the resulting image for a 300×300 μm^2 detector.

The detector in question is missing a portion of the metal contact, which helps to illustrate the results of the measurement: exposed areas glow with an intensity that directly correlates to the efficiency of carrier collection when carriers are generated at that location. It is clear from the EBIC image that the collection of generated carriers is far from uniform. Image processing software was used to analyze the current collection profile at points on top of the detector. Line profiles were averaged horizontally over the rectangular area shown in the EBIC image of Figure 4.3. As seen in the plot, the collected current falls to levels comparable to the current collected when the beam is incident on the metal contact. This suggests that the generation-recombination processing occuring within the device prevent current from being collected from every portion of the detector, especially for larger devices. This means that the derived figures of merit (R_0A, R, D*) are all sub-optimal. The results can be improved by altering the device design to minimize the greatest distance from any given portion of the contact. Improving the quality of carrier transport will also result in more uniform collection. The experiment can also be improved by using Monte Carlo simulation [33] to model the carrier generation volume and derive the minority carrier lifetimes based on the measured profiles.

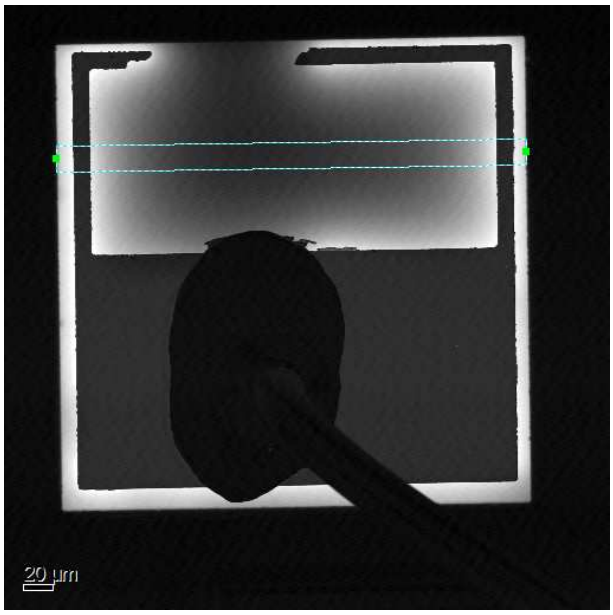

(a)

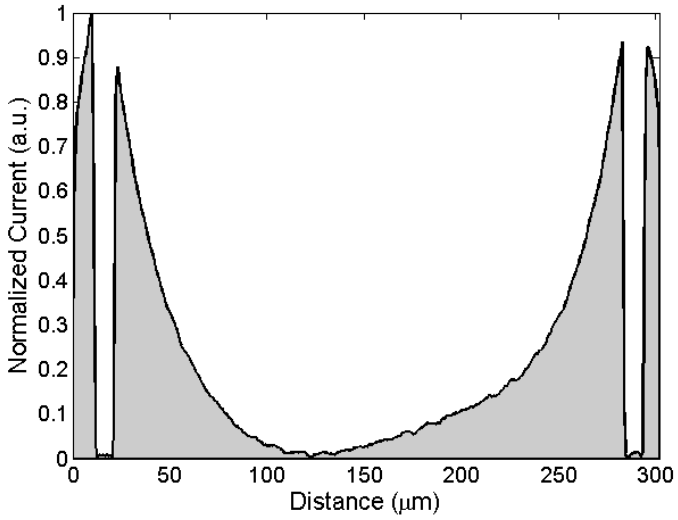

(b)

Figure 4.3: (Top) EBIC imaging of a typical InAs/GaSb T2SL detector (300×300 μm^2). The exposed areas of the detector have a white level corresponding to the efficiency of current collection when the electron beam is placed at that location. A smaller rectangle shows the region that is processed to generate a line profile. (Bottom) The resulting normalized line scan, obtained using digital image processing software. Near the middle of the central optical area, the collected current falls to near zero. The asymmetry of the profile derives from the missing contact in the upper portion of the detector.

Chapter 5

Conclusion

5.1 Summary

In this work, novel T2SL structures were grown via metalorganic chemical vapor deposition and studied. The major achievement is the demonstration of the first T2SL detectors grown on InAs substrates, realized via MOCVD growth. The improvement in D^* is a very encouraging result for MOCVD growth, although the value is still inferior to state-of-the-art devices grown by MBE. Nonetheless, the results demonstrate the advantages of using InAs substrates for improvements in MOCVD-grown detector performance. A wide range of characterization methods have yet to be realized to their full potential in T2SL applications, including electron beam induced current and capacitance-voltage measurement. Future work should focus on the improvement of MOCVD growth as well as the design of advanced T2SL structures for higher performance via MOCVD growth and for advanced characterization to gain understanding of the nature of defects and other limiting factors in detector performance.

5.2 Future Work

5.2.1 Advanced T2SL IR Photodiodes on InAs Substrates

The demonstration of InAs substrates in MOCVD-grown T2SL photodiodes marks just the beginning of a very promising avenue for future detectors that are grown via MOCVD. Further work is necessary to demonstrate the full capabilities of MOCVD growth on InAs substrates and improve device performance so that the results are competitive with comparable MBE-grown

products. Further investigation of interfacial layers should be performed in order to determine the optimal conditions for SL growth. The use of ternary compounds in the SL structure should provide greater tunability through the control of the material bandgap of a compound such as $In_xGa_{1-x}Sb$ or $InAs_xSb_{1-x}$. While ternary T2SL devices have been demonstrated on InAs substrates in the past [34, 35] for laser applications, their potential has yet to be explored for long-wavelength detector applications, especially via MOCVD. In addition, novel device structures like those discussed in Chapter 1 should also be investigated to improve detector performance. Advanced processing techniques, including surface passivation with electrically inactive materials, should also be useful given the observed effects of low surface resistivity. Lastly, there still remains room for innovative and unconventional approaches to T2SL IR photodetector designs. Optical elements, including deposited metal and distributed Bragg reflectors, can be implemented to enhance the effective optical absorption of a detector. Refractive elements can be used to improve the solid angle of detection of a detector, increasing the versatility of use.

In addition to the advancement of T2SL detectors, there is additional work that can be done to improve upon the characterization of their performance. Two such applications that show promise are detailed below.

5.2.2 Cross-Sectional EBIC Measurement

A more advanced application of EBIC is to use the generation volume of the electron beam to influence current generation near the depletion region of a doped structure. If the electron beam incidence is perpendicular to the direction of growth, the position of the beam with respect to the depletion region can be used to determine the amount of current collected based on the diffusion length of the generated minority carriers and the expected geometry of the generation volume [33, 36, 37]. By modeling the expected current generation profile as the beam moves across the depletion region and fitting to experimental data, the carrier diffusion parameters can be modeled. This process has previously been demonstrated on T2SL IR photodiodes grown via MBE [37], but the technique will remain important for future study of carrier lifetimes in more advanced structures grown via MOCVD and to verify the

efficacy of passivation techniques that reduce the effects of surface defects. Additional refinement of the theoretical model will also improve the accuracy of the extracted parameters and provide novel observations.

5.2.3 Capacitance-Voltage Study

Another potentially useful tool for characterizing the behavior of defect states involves measuring the transient response of capacitance to periodic pulses in voltage [38], a technique called deep-level transient spectroscopy (DLTS). For example, if a device is held in reverse bias the active trap states in the depletion region will be vacated due to the strong electric field that removes ejected carriers. If a forward bias voltage is pulsed, the trap states will be saturated due to an influx of carriers. When the device returns to reverse bias, the carriers evacuate based on the lifetime of the trap states that hold them. This change in charge occupation levels manifests as a shift in the depletion region, which in turn can be measured as capacitance. Using a lock-in amplifier [39] and a fast capacitance measurement system, the variance of the capacitance can be measured to extract the recombination parameters of the carriers within active defects. DLTS has been demonstrated to be capable of detecting trap energy levels in SL samples [40, 41], although it has yet to receive attention as a method of study for T2SL IR detectors, since the observation of traps with short lifetimes can be difficult. Currently T2SL IR detectors exhibit lifetimes on the order of hundreds of nanoseconds, meaning that investigation into advanced measurement techniques will be necessary to demonstrate the viability of DLTS until the performance of the SL structures can be improved. Possible avenues of investigation include avalanche detection methods to artificially lengthen lifetime, passivation methods to improve carrier lifetime, and the use of band structure engineering to suppress recombination and/or decrease carrier emission probabilities.

References

[1] "Atmospheric transmission chart." [Online]. Available: http://www.globalwarmingart.com/images/7/7c/Atmospheric_Transmission.png

[2] A. Jha, *Infrared Technology*. New York: Wiley, 2000.

[3] A. Rogalski, *Infrared detectors*, ser. Electrocomponent science monographs. New York, NY: Gordon & Breach, 2000.

[4] D. L. Smith and C. Mailhiot, "Proposal for strained type II superlattice infrared detectors," *Journal of Applied Physics*, vol. 62, no. 6, p. 2545, 1987.

[5] A. Rogalski, "Recent progress in infrared detector technologies," *Infrared Physics & Technology*, Dec. 2010.

[6] J. D. Vincent, *Fundamentals of Infrared Detector Operation and Testing*. New York, NY: Wiley-Interscience, 1990.

[7] S. Chuang, *Physics of Photonic Devices*, 2nd ed. Hoboken, NJ: Wiley, 2009.

[8] S. Mou, J. V. Li, and S. L. Chuang, "Surface channel current in InAs-GaSb type-II superlattice photodiodes," *Journal of Applied Physics*, vol. 102, no. 6, p. 066103, Sep. 2007.

[9] A. Hood, M. Razeghi, E. H. Aifer, and G. J. Brown, "On the performance and surface passivation of type II InAsGaSb superlattice photodiodes for the very-long-wavelength infrared," *Applied Physics Letters*, vol. 87, no. 15, p. 151113, Oct. 2005.

[10] L. Esaki and R. Tsu, "Superlattice and negative differential conductivity in semiconductors," *IBM Journal of Research and Development*, vol. 14, no. 1, pp. 61–65, Jan. 1970.

[11] W. Tennant et al., "MBE HgCdTe technology: A very general solution to IR detection, described by "Rule 07", a very convenient heuristic," *Journal of Electronic Materials*, vol. 37, no. 9, pp. 1406–1410, Mar. 2008.

[12] I. Vurgaftman et al., "Analysis and performance of type-II superlattice infrared detectors," *Optical Engineering*, vol. 50, no. 6, p. 061007, 2011.

[13] P.-Y. Delaunay, B. M. Nguyen, D. Hoffman, E. K.-W. Huang, and M. Razeghi, "Background limited performance of long wavelength infrared focal plane arrays fabricated from M-structure InAsGaSb superlattices," *IEEE Journal of Quantum Electronics*, vol. 45, no. 2, pp. 157–162, Feb. 2009.

[14] B.-M. Nguyen, S. Bogdanov, S. A. Pour, and M. Razeghi, "Minority electron unipolar photodetectors based on type II InAs/GaSb/AlSb superlattices for very long wavelength infrared detection," *Applied Physics Letters*, vol. 95, no. 18, p. 183502, Nov. 2009.

[15] S. Maimon and G. W. Wicks, "nBn detector, an infrared detector with reduced dark current and higher operating temperature," *Applied Physics Letters*, vol. 89, no. 15, p. 151109, Oct. 2006.

[16] A. Khoshakhlagh et al., "Long wavelength InAs/GaSb superlattice detectors based on nBn and pin design," *Proceedings of SPIE*, vol. 7298, no. 1, pp. 72 981P–72 981P–7, May 2009.

[17] J. B. Rodriguez et al., "nBn structure based on InAsGaSb type-II strained layer superlattices," *Applied Physics Letters*, vol. 91, no. 4, p. 043514, 2007.

[18] D. Z.-Y. Ting et al., "A high-performance long wavelength superlattice complementary barrier infrared detector," *Applied Physics Letters*, vol. 95, no. 2, p. 023508, July 2009.

[19] I. Vurgaftman et al., "Graded band gap for dark-current suppression in long-wave infrared W-structured type-II superlattice photodiodes," *Applied Physics Letters*, vol. 89, no. 12, p. 121114, Sep. 2006.

[20] A. Petschke, M. Mandl, S. Chuang, Y. Huang, J. Ryou, and R. Dupuis, "Metal-organic chemical vapour deposition growth of InAs/GaSb type-II superlattice photodiodes," *Electronics Letters*, vol. 46, no. 16, pp. 1151–1152, Aug. 2010.

[21] Y. Huang, J.-H. Ryou, R. D. Dupuis, A. Petschke, M. Mandl, and S.-L. Chuang, "InAs/GaSb type-II superlattice structures and photodiodes grown by metalorganic chemical vapor deposition," *Applied Physics Letters*, vol. 96, no. 25, p. 251107, 2010.

[22] E. Schubert, *Light-Emitting Diodes*, 2nd ed. Cambridge, UK: Cambridge University Press, 2006.

[23] G. Liu and S.-L. Chuang, "Modeling of Sb-based type-II quantum cascade lasers," *Physical Review B*, vol. 65, no. 16, Apr. 2002.

[24] S. Chuang and C. Chang, "kp method for strained wurtzite semiconductors," *Physical Review B*, vol. 54, no. 4, pp. 2491–2504, July 1996.

[25] M. Mandl, "Antimony-based type-II superlattice infrared detectors," Ph.D. dissertation, University of Illinois at Urbana-Champaign, May 2010.

[26] A. Soibel et al., "High-performance long wavelength superlattice infrared detectors," *Proceedings of SPIE*, vol. 7945, no. 1, p. 79451P, 2011.

[27] E. Plis et al., "Mid-infrared InAs/GaSb strained layer superlattice detectors with nBn design grown on a GaAs substrate," *Semiconductor Science and Technology*, vol. 25, no. 8, p. 085010, Aug. 2010.

[28] J. J. Lander, H. Schreiber, T. M. Buck, and J. R. Mathews, "Microscopy of internal crystal imperfections in Si p-n junction diodes by use of electron beams," *Applied Physics Letters*, vol. 3, no. 11, p. 206, Nov. 1963.

[29] W. Seifert, M. Kittler, and J. Vanhellemont, "EBIC study of recombination activity of oxygen precipitation related defects in Si," *Materials Science and Engineering: B*, vol. 42, no. 1-3, pp. 260–264, Dec. 1996.

[30] T. Sekiguchi, B. Shen, T. Watanabe, and K. Sumino, "EBIC study on the electrical activity of stacking faults in silicon," *Materials Science and Engineering: B*, vol. 42, no. 1-3, pp. 235–239, Dec. 1996.

[31] M. Kittler and W. Seifert, "On the origin of EBIC defect contrast in silicon. A reflection on injection and temperature dependent investigations," *Physica Status Solidi (a)*, vol. 138, no. 2, pp. 687–693, Aug. 1993.

[32] L. Marton, "Experiments on low-energy electron scattering and energy losses," *Reviews of Modern Physics*, vol. 28, no. 3, pp. 172–183, July 1956.

[33] J.-M. Bonard and J.-D. Ganiere, "Quantitative analysis of electron-beam-induced current profiles across pn junctions in GaAs/Al0.4Ga0.6As heterostructures," *Journal of Applied Physics*, vol. 79, no. 9, p. 6987, 1996.

[34] Y.-H. Zhang, R. Miles, and D. Chow, "InAs-InAs/sub x/Sb/sub 1-x/ type-II superlattice midwave infrared lasers grown on InAs substrates," *IEEE Journal of Selected Topics in Quantum Electronics*, vol. 1, no. 2, pp. 749–756, June 1995.

[35] S. R. Kurtz, A. A. Allerman, and R. M. Biefeld, "Midinfrared lasers and light-emitting diodes with InAsSb/InAsP strained-layer superlattice active regions," *Applied Physics Letters*, vol. 70, no. 24, p. 3188, 1997.

[36] Z. Z. Bandic, P. M. Bridger, E. C. Piquette, and T. C. McGill, "Minority carrier diffusion length and lifetime in GaN," *Applied Physics Letters*, vol. 72, no. 24, p. 3166, 1998.

[37] J. V. Li, S. L. Chuang, E. M. Jackson, and E. Aifer, "Minority carrier diffusion length and lifetime for electrons in a type-II InAsGaSb superlattice photodiode," *Applied Physics Letters*, vol. 85, no. 11, p. 1984, Sep. 2004.

[38] A. Rohatgi, J. Davis, R. Hopkins, and P. McMullin, "A study of grown-in impurities in silicon by deep-level transient spectroscopy," *Solid-State Electronics*, vol. 26, no. 11, pp. 1039–1051, Nov. 1983.

[39] D. S. Day, M. Y. Tsai, B. G. Streetman, and D. V. Lang, "Deep-level-transient spectroscopy: System effects and data analysis," *Journal of Applied Physics*, vol. 50, no. 8, p. 5093, July 1979.

[40] D. Stievenard, D. Vuillaume, J. C. Bourgoin, B. Deveaud, and A. Regreny, "Defects in Superlattices," *Europhysics Letters (EPL)*, vol. 2, no. 4, pp. 331–335, Aug. 1986.

[41] S. Q. Wang et al., "Electronic states in ZnSe/ZnTe type-II superlattice studied by capacitance transient spectroscopy," *Journal of Applied Physics*, vol. 82, no. 7, p. 3402, 1997.